Supporting Information

Synergy of Diatomic CuSb-HAB Catalyst with Methanol Oxidation to Promote Formamide Electrosynthesis

Xuezi Xing, Dong Zhang, Yunhe Li, Xiaomei Wang, Xing Yang *, Ke Chu *

School of Materials Science and Engineering, Lanzhou Jiaotong University, Lanzhou 730070, China

*Corresponding author. E-mail: yangxing@mail.lzjtu.cn (X. Yang), chukelut@126.com (K. Chu)

Experimental Section

Synthesis of Cu-HAB and CuSb-HAB

All reagents involved in this study were commercially available and used without further purification. $CuSO_4 \cdot 5H_2O$ (54 mg, 0.22 mmol), NH_4OH (14 M, 1.4 mL) and HAB hydrochloride (40 mg, 0.144 mmol) were co-added into a degassed DMSO (6 mL) solution, which was then kept at 60 ℃ for 8 h under magnetic stirring. After cooling, the precipitated were collected by by centrifuging, washing with deionized water/acetone, and drying under vacuum, obtaining Cu-HAB. Subsequently, $SbCl_3$ (2 mg) was dissolved in degassed ethanol, followed by adding Cu-HAB (10 mg). The mixture was then stirred at 60 ℃ for 12 h and the precipitated were collected by by centrifuging, washing with deionized water/methanol and freeze-drying overnight to obtain CuSb-HAB MOF.

Electrochemical experiments in flow cell

The electrochemical measurements were conducted in a commercial flow cell electrolyzer. To prepare the catalyst ink, 25 mg of the catalyst was dispersed in 3 mL of isopropanol, followed by the addition of 20 μL of a 5 wt% Nafion ionomer aqueous solution. This ink was then uniformly coated onto a sheet of carbon paper using a drop-casting method, achieving a target catalyst loading of approximately 0.5 mg cm^{-2} to fabricate the gas diffusion electrode (GDE). The electrochemical cell configuration employed a nickel mesh as the anode and an Ag/AgCl electrode as the reference electrode. The cathode and anode compartments were separated by a proton exchange membrane (Nafion N117, product code 171001). All reported electrode potentials were converted to the reversible hydrogen electrode (RHE) scale using the formula: E (V vs. RHE) = E (V vs. Ag/AgCl) + 0.198 V + 0.059 × pH. The cathode chamber was filled with an electrolyte containing 0.02 M KNO_2 and 0.2 M $KHCO_3$, while the anode chamber contained a 1 M KOH solution. For the anodizing process, the anodic solution was replaced with a mixture of 1.0 M CH_3OH and 1.0 M KOH. Prior to electrochemical testing, the catholyte was saturated by purging with either

CO_2 or Ar gas. During the CO_2 reduction electrolysis, CO_2 gas was continuously supplied to the back side of the GDE (the side without catalyst) at a controlled flow rate of 20 standard cubic centimeters per minute (s.c.c.m.). Simultaneously, both the catholyte and anolyte solutions were circulated through their respective chambers at a flow rate of 20 mL min^{-1} using pumps.

Electrochemical experiments in MEA cell

For the two-electrode ECNF||MOR, the MEA consisted of a gas diffusion cathode (CuSb-HAB@GDE), an anion exchange membrane (Sustainion X37-50 Grade RT) as well as a commercial Pt/C anode. On the cathode side, humid CO_2 was continuously supplied at a flow rate of 30 ml min^{-1}. At the anode side, an electrolyte of 1 M KOH with 1 M CH_3OH was circulated using a peristaltic pump at a flow rate of 50 ml min^{-1}. The anode electrolyte was replenished periodically during the long-term stability tests to ensure an adequate supply of CH_3OH.

Determination of formamide

The identification and quantification of formamide and other liquid products in C-N coupling electrosynthesis were conducted using the ^1H NMR method[1]. Approximately 400 μL liquid sample was mixed with 200 μL DMSO-d6 solution (D-99.9%, Cambridge Isotope Laboratories), then the solution was tested in a 600 MHz ^1H 1D liquid NMR spectrometer (Bruker Advance) equipped by cryoprobe for 512 scans. The 1D ^1H spectrum was measured with water suppression excitation sculpting method. External standard method with 10 mmol mL^{-1} disodium maleate solution (Sigma-Aldrich, ≥98%) was used for quantification.

The formamide yield rates (YR_{FA}) and Faradaic efficiency (FE_{FA}) were calculated by the following equation:

$$YR_{FA}\ (\text{mmol h}^{-1}\text{cm}^{-2}) = \frac{c_{FA} \times V}{45.04 \times t \times A} \quad (1)$$

$$FE_{FA} = \frac{n \times F \times c_{FA} \times V}{M \times Q} \times 100\% \quad (2)$$

where c_{FA} (μg mL^{-1}) is the measured formamide concentration, V (mL) is the volume of the electrolyte, t (h) is the reduction time, A (cm^{-2}) is the surface area of cathode, F (96 500 C mol^{-1}) is the Faraday constant, Q (C) is the quantity of applied electricity.

Determination of NH_3

NH_3 in electrolyte was quantitatively determined by the indophenol blue method[2]. Typically, 2 mL of electrolyte was removed from the electrochemical reaction vessel and diluted with deionized water. Then 2 mL of diluted solution was removed into a clean vessel followed by sequentially adding NaOH solution (2 mL, 1 M) containing $C_7H_6O_3$ (5 wt.%) and $C_6H_5Na_3O_7$ (5 wt.%), NaClO (1 mL, 0.05 M), and $C_5FeN_6Na_2O$ (0.2 mL, 1wt.%) aqueous solution. After the incubation for 2 h at room temperature, the mixed solution was subjected to UV-vis measurement using the absorbance at 655 nm wavelength. The concentration-absorbance curves were calibrated by the standard NH_4Cl solution with a series of concentrations.

Determination of NO_2^-

NO_2^- in electrolyte was determined by a Griess test[3]. Typically, 2 mL of electrolyte was removed from the electrochemical reaction vessel and diluted with deionized water. The coloring solution was prepared by dissolving N-(1-naphthyl) ethylenediamine dihydrochloride (0.1 g), sulfonamide (1.0 g) and H_3PO_4 (2.94 mL, 85%) into 50 mL of deionized water. Add 0.1 mL of coloring solution to the diluted electrolyte. After incubation for 30 min at room temperature, the mixture was subjected to UV-vis measurements and the absorption spectrum (range 400–700 nm) was obtained. The absorbance at 540 nm was measured to determine the concentration of generated $NO_2^-$with a standard curve of $NaNO_2$.

Characterizations

Inductively coupled plasma optical emission spectroscopy (ICP-OES) was performed on a PerkinElmer AVIO 500 spectrometer. X-ray diffraction (XRD) pattern was collected on a Rigaku D/max 2400 diffractometer with Cu Kα radiation (λ =1.5418 Å, 40 kV). Transmission electron microscopy (TEM) was performed on a

Tecnai G^2 F20 microscope. Aberration-corrected scanning transmission electron microscopy (AC-STEM) was performed on a Titan Cubed Themis G^2 300 microscope. X-ray photoelectron spectroscopy (XPS) analysis was conducted on a PHI 5702 spectrometer. Online differential electrochemical mass spectrometry (DEMS, QAS 100) was performed by QAS 100 spectrometer. In situ FTIR measurements were performed on a Nicolet 6700 FT-IR spectrometer.In situ Raman spectroscopy analysis was carried out on a confocal Raman spectrometer (Horiba HR-800) with a wavelength of 532 nm.

Calculation details

DFT calculations were carried out using the Cambridge sequential total energy package (CASTEP) with ultrasoft pseudopotentials. The exchange-correlation functional is evaluated using the Perdew-Burke-Ernzerhof (PBE) in the generalized gradient approximation. DFT-D3 method was employed to calculate the van der Waals (vdW) interactions. According to the experimental characterizations, pristine Cu has been modeled as 2 × 2 supercell of CuSb-HAB (001) surface with four atomic layers. A vacuum region of 18 Å was used to separate adjacent slabs. The cutoff energy was set as 400 eV and the k-point meshes were set as 3 × 3 × 1. The AIMD simulation was carried out to estimate the thermal stability, in which the NVT ensemble is chosen with the total simulation time of 5 ns at a time step of 1 fs.

The computational hydrogen electrode (CHE) model was adopted to calculate the Gibbs free energy change (ΔG) for each elementary step as follows:

$$\Delta G = \Delta E + \Delta E_{ZPE} - T\Delta S \quad (3)$$

where ΔE represents the electronic energy contribution directly derived from DFT calculations. ΔE_{ZPE} and $T\Delta S$ denote the contributions of zero-point energy and entropy (at 298.15 K), respectively. These values can be obtained from the NIST database for free molecules.

Molecular dynamics (MD) simulations were performed using the Forcite module. The electrolyte system was modeled by a cubic cell with placing catalyst at the center

of the cell and randomly filling 1000 H_2O, 50 NO_2^-, 20 CO_2 molecules, and 50 H atoms. The force field type was chosen as universal. After geometry optimization, the MD simulations were performed in an NVT ensemble (298 K) with the total simulation time of 5 ns at a time step of 1 fs.

The radial distribution function (RDF) is calculated by:

$$g(r) = \frac{dN}{4\pi\rho r^2 dr} \tag{4}$$

where dN is the amount of molecules in the shell between the central particle r and $r+dr$, ρ is the number density of NO_2^-, CO_2, H_2O and H.

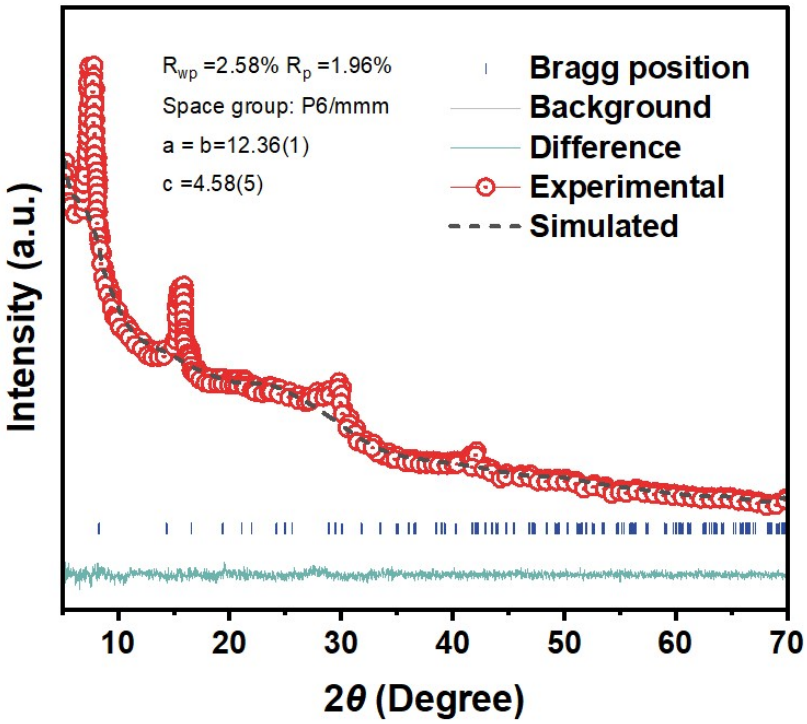

Figure S1. Rietveld Refinement results of PXRD pattern of CuSb-HAB.

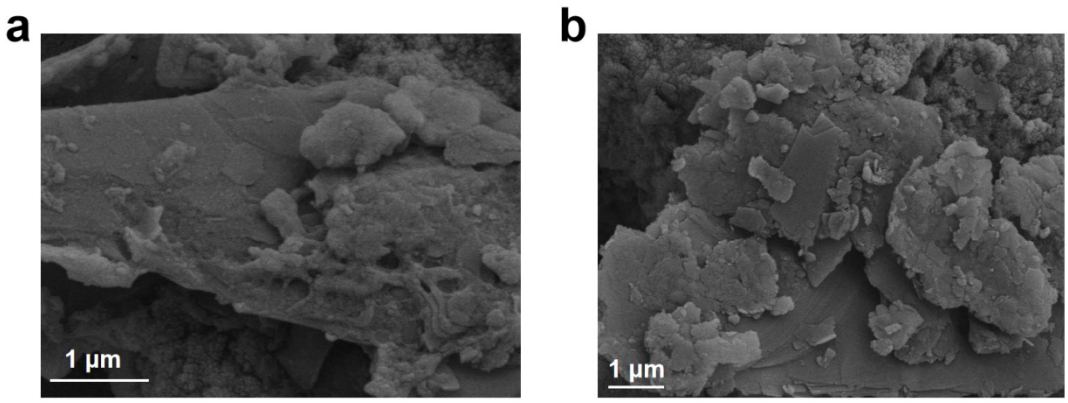

Figure S2. SEM images of (a) Cu-HAB and (b) CuSb-HAB.

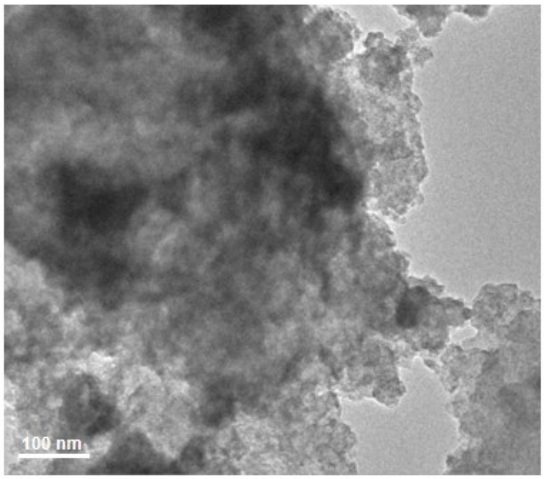

Figure S3. TEM image of Cu-HAB.

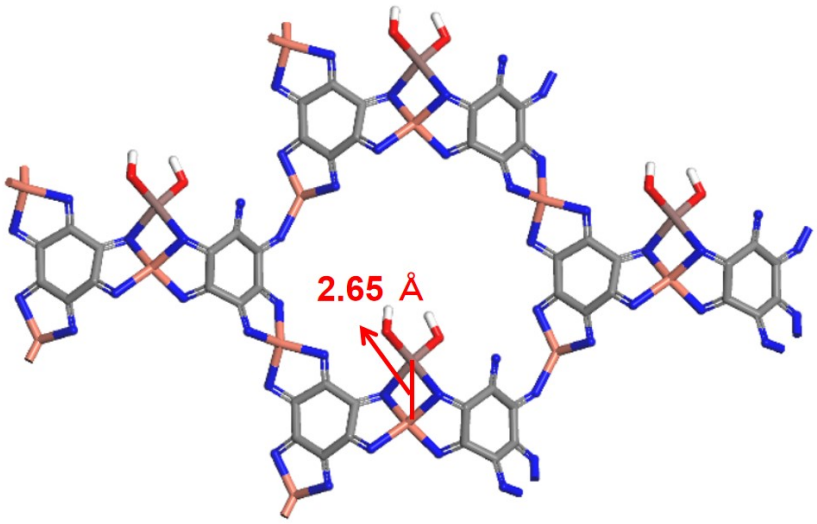

Figure S4. Calculated structure model of CuSb-HAB.

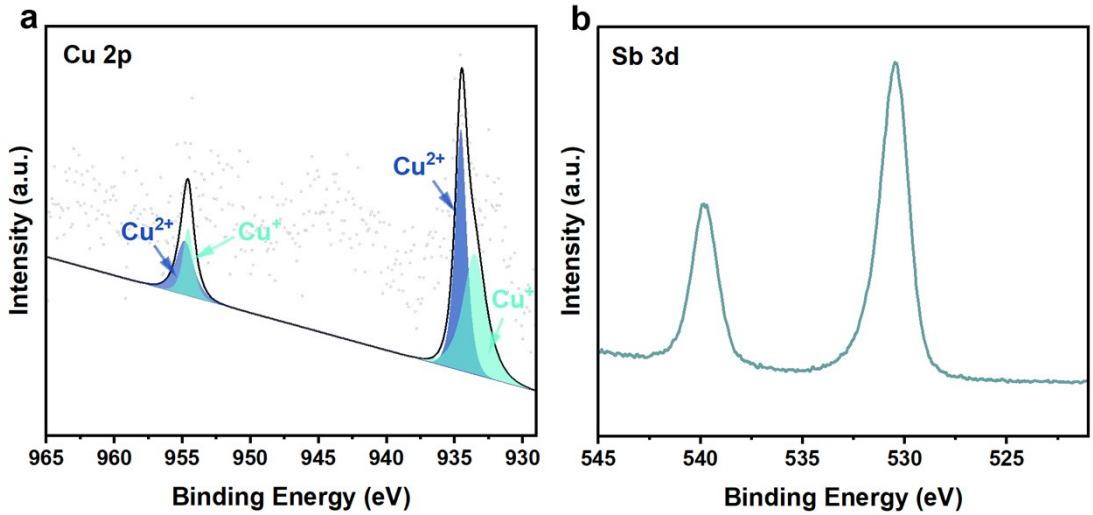

Figure S5. (a) Cu 2p and (b) Sb 3d spectra of CuSb-HAB.

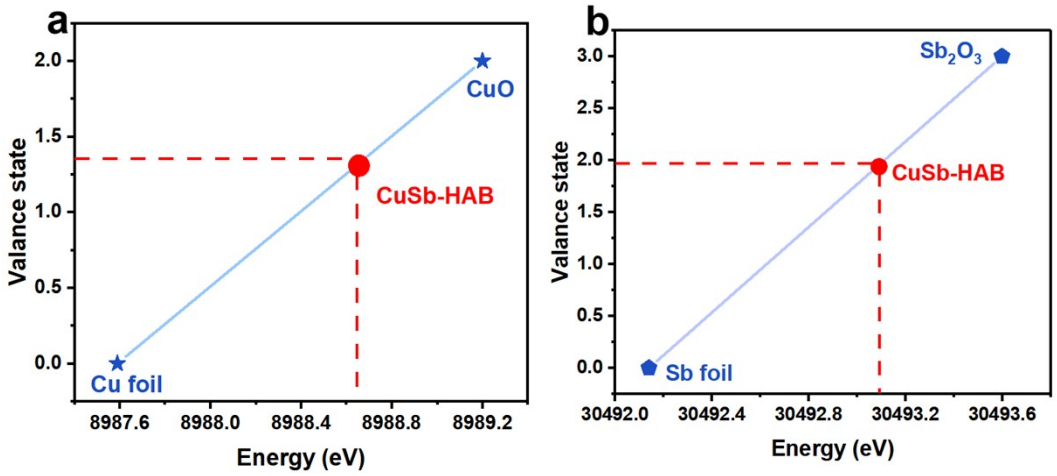

Figure S6. (a) Linear Cu K-edge XANES fitting curve of CuSb-HAB. (b) Linear Sb K-edge XANES fitting curve of CuSb-HAB.

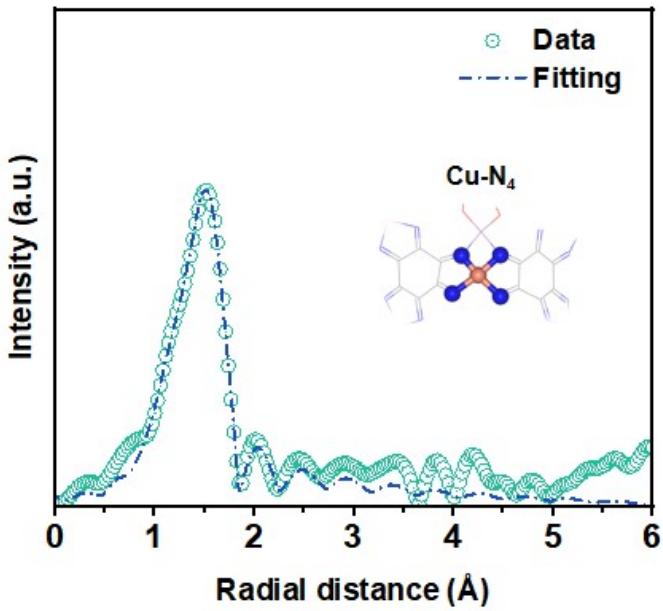

Figure S7. EXAFS fitted curve of CuSb-HAB (inset: fitted model).

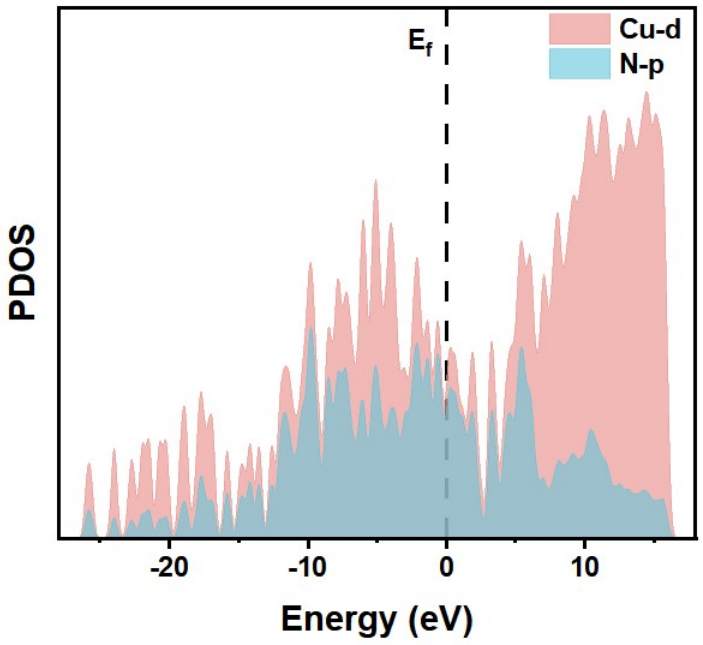

Figure S8. PDOS profile of CuSb-HAB.

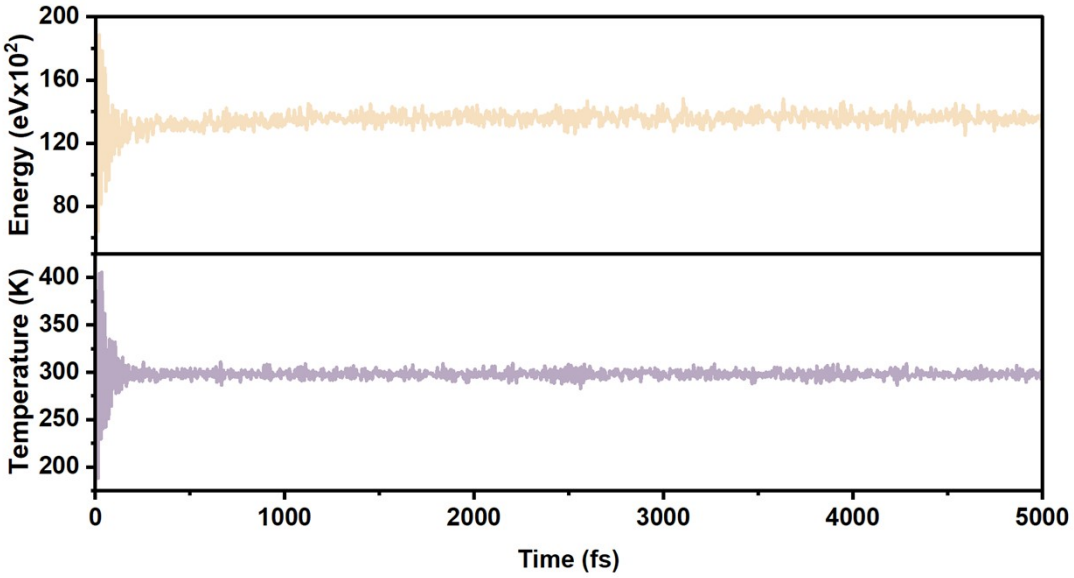

Figure S9. Energy and temperature variations during the AIMD simulation of CuSb-HAB for 5 ns.

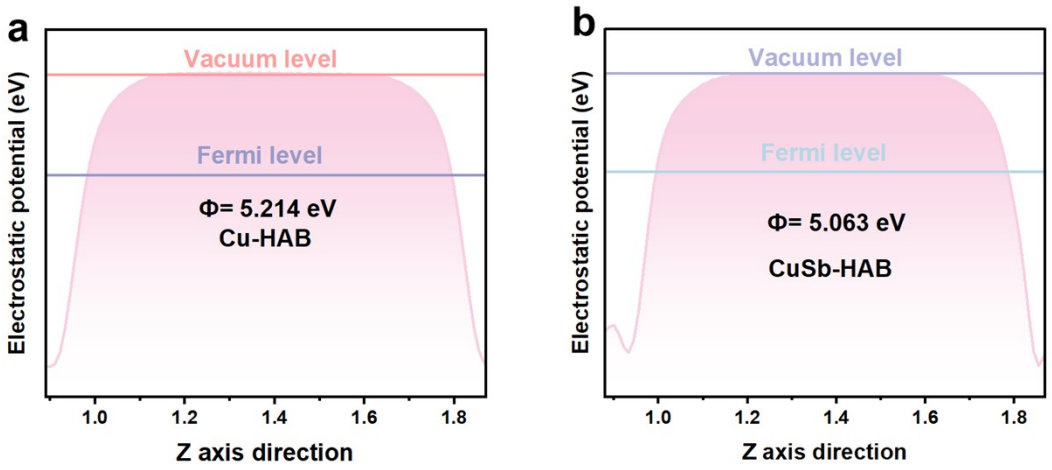

Figure S10. Average potential profiles along z-axis direction for calculating the work functions of (a) Cu-HAB and (b) CuSb-HAB.

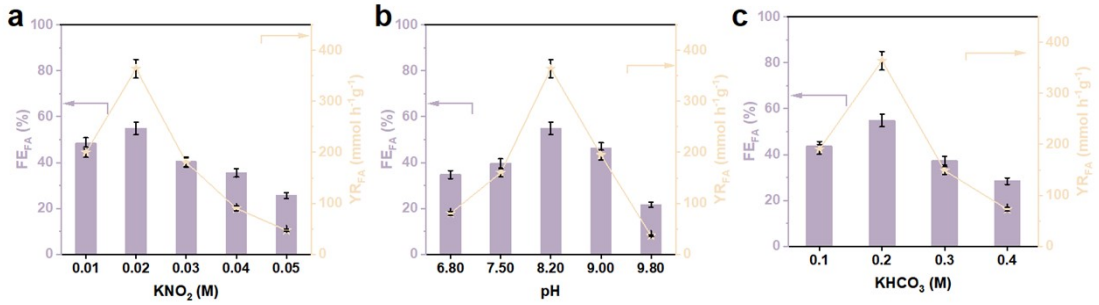

Figure S11. (a) YR_{FA} and FE_{FA} after 1 h electrolysis on CuSb-HAB with varying KNO_2 concentrations (0.01, 0.02, 0.03, 0.04 and 0.05 M). (b) YR_{FA} and FE_{FA} after 1 h electrolysis on CuSb-HAB with varying pH values (6.80, 7.50, 8.20, 9.00 and 9.80). (c) YR_{FA} and FE_{FA} after 1 h electrolysis on CuSb-HAB with varying $KHCO_3$ concentrations (0.1, 0.2, 0.3 and 0.4 M).

The optimal nitrite concentration is 0.02 M in 0.2 M $KHCO_3$, yielding the highest FE_{FA} of 54.9% and a YR_{FA} of 376 mmol h^{-1} g^{-1}, while low concentrations limit $*NH_2$ formation and high concentrations cause competitive adsorption of excess NO_2^- and promote over-reduction to NH_3, both reducing the formamide selectivity (Figure S11a). The optimal pH is near-neutral/weakly alkaline (pH ≈ 8.2, corresponding to 0.2 M $KHCO_3$), as acidic conditions suppress *CHO formation via enhanced HER and CO_2 conversion to HCO_3^-, and strongly alkaline conditions hinder adsorption and reduce its solubility, lowering C-N coupling efficiency (Figure S11b). Low buffer concentrations fail to prevent local alkalization and favor HER and NRA, while high buffer concentrations increase ionic strength, impeding CO_2 mass transport and reducing overall activity. As such, 0.2 M $KHCO_3$ provides optimal buffering to stabilize the local pH (Figure S11c).

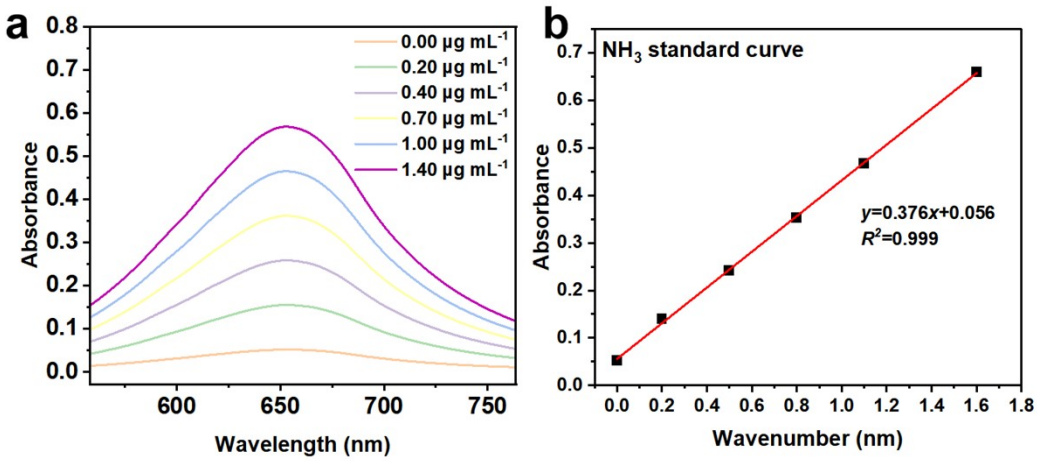

Figure S12. (a) UV-vis absorption spectra of NH_4Cl assays after incubated for 2 h at ambient conditions. (b) Calibration curve used for the calculation of NH_3 concentrations.

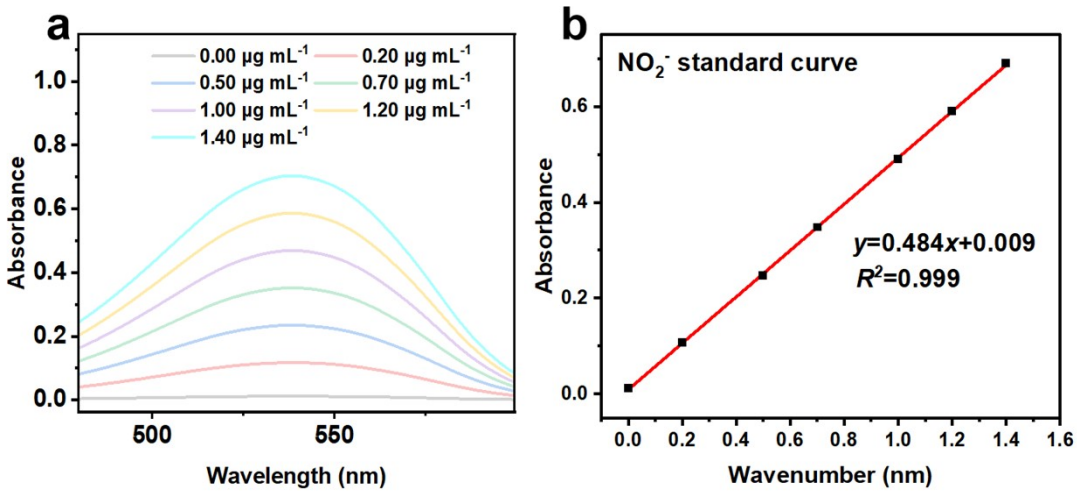

Figure S13. (a) UV-vis absorption spectra of NO_2^- assays after incubated for 20 min at ambient conditions. (b) Calibration curve used for calculation of NO_2^- concentrations.

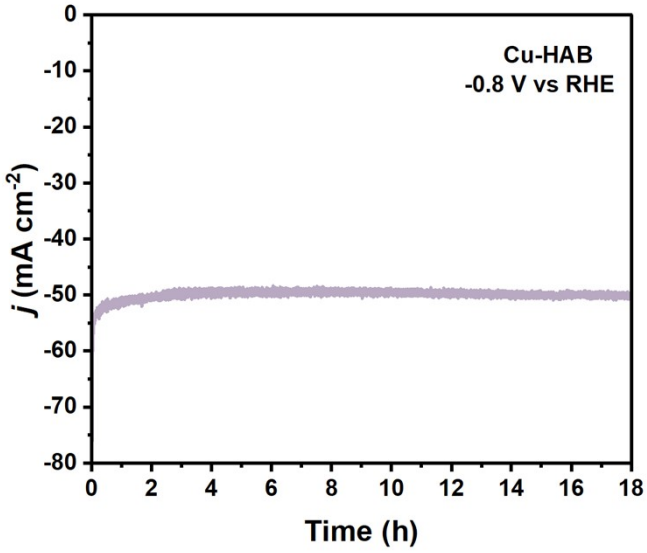

Figure S14. Chronoamperometry test of Cu-HAB at -0.8 V in flow cell.

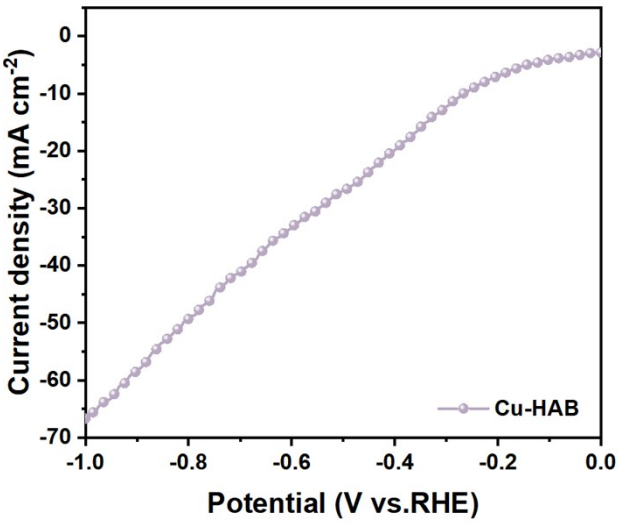

Figure S15. LSV curve of Cu-HAB in flow cell.

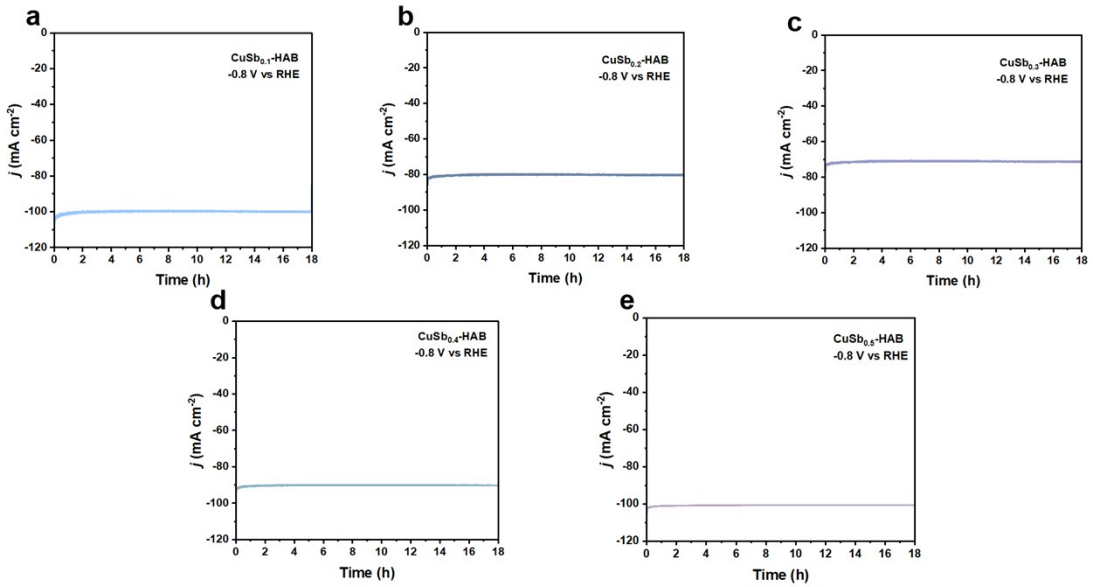

Figure S16. Chronoamperometry test of $CuSb_x$-HAB with varying Sb contents (x=0.1,0.2,0.3,0.4 and 0.5) at -0.8 V vs RHE in flow cell.

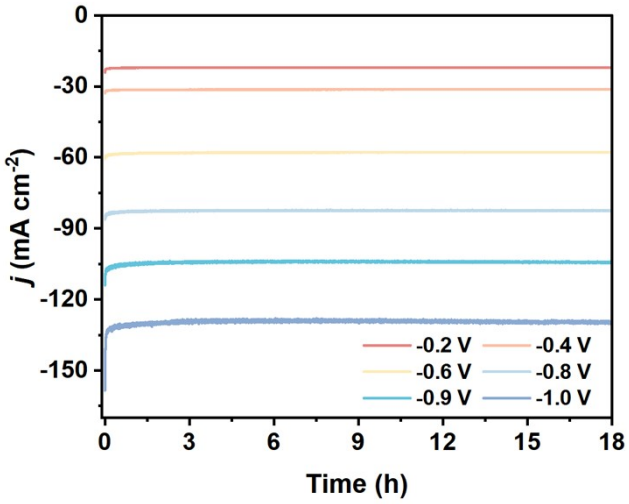

Figure S17. Chronoamperometry test of $CuSb_{0.2}$-HAB at different potentials in flow cell.

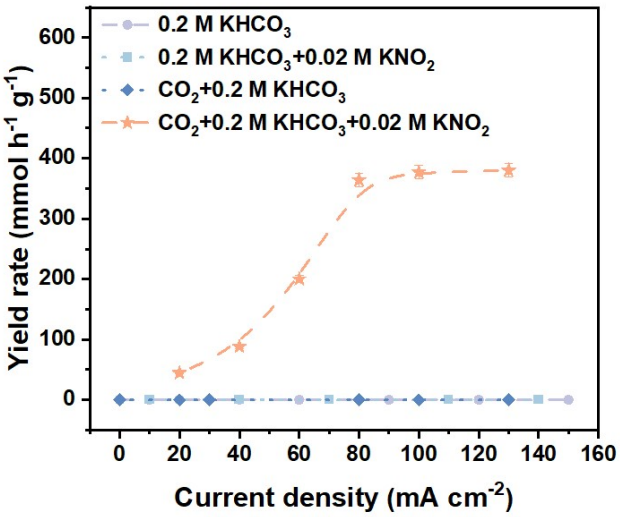

Figure S18. YR_{FA} of CuSb-HAB in different electrolytes .

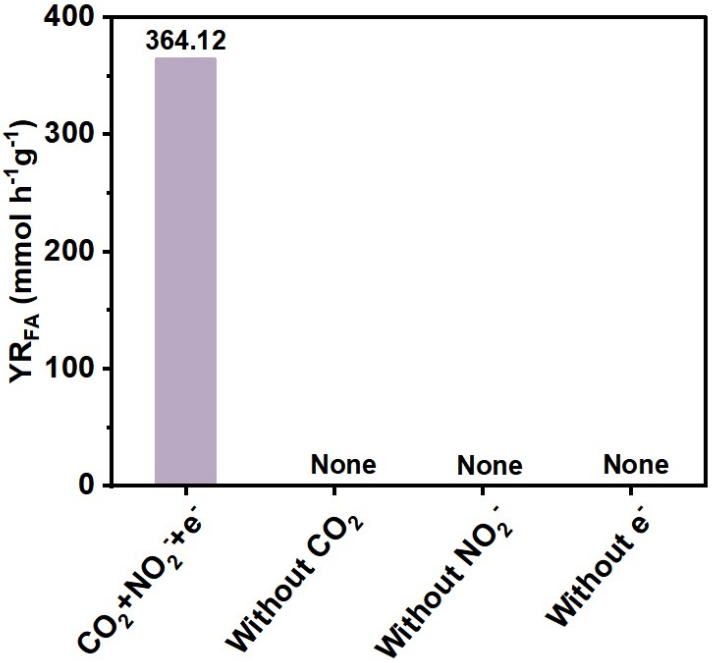

Figure S19. Amounts of produced formamide on CuSb-HAB under different conditions: (1) electrolysis in NO_2^- and CO_2 containing solution at -0.8 V, (2) electrolysis in NO_2^- free electrolyte at -0.8 V, (3) electrolysis in CO_2-saturated at -0.8 V, (4) electrolysis in $NO_2^-$and CO_2-containing solution at OCP.

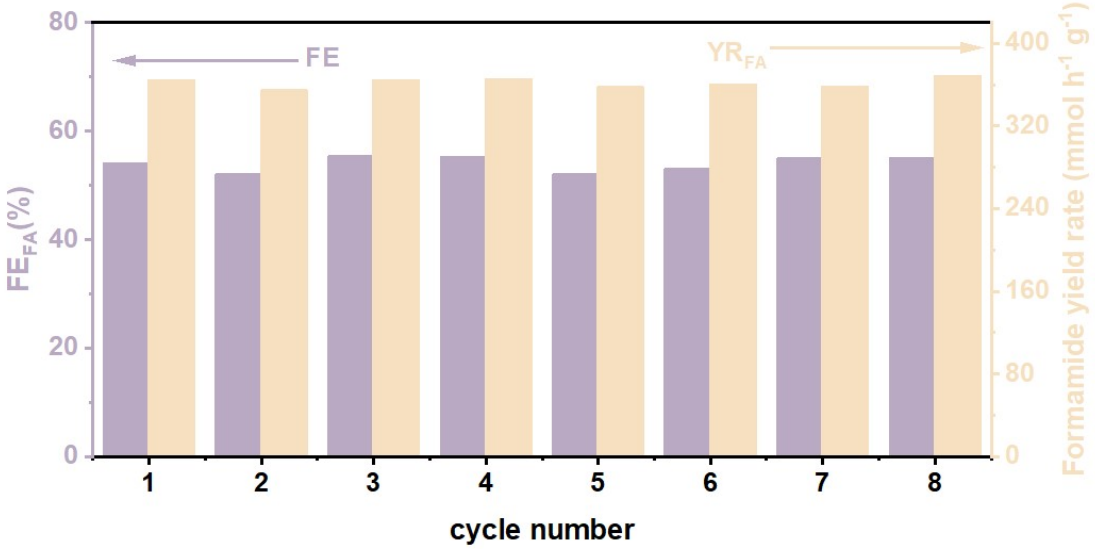

Figure S20. Cycling test of CuSb-HAB in flow cell at -0.8 V.

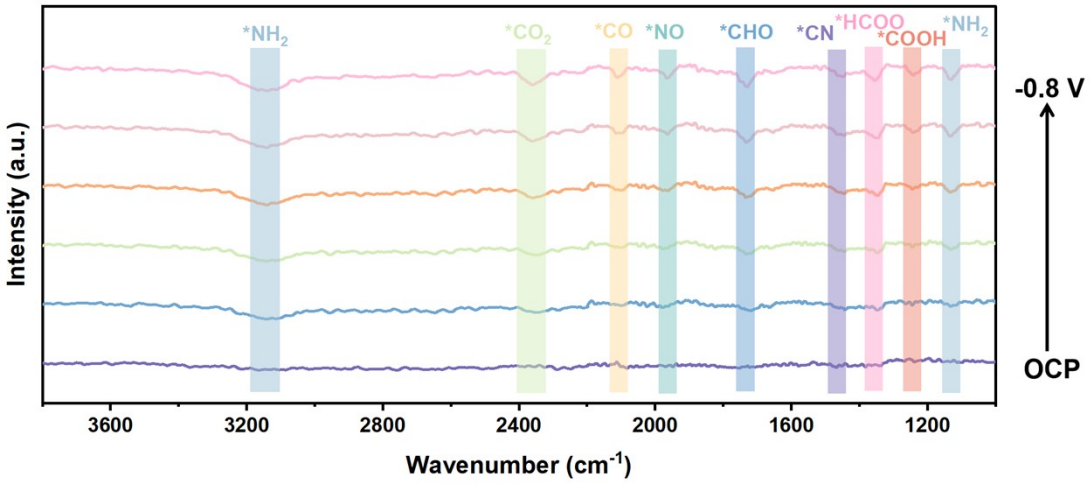

Figure S21. Potential-dependent in situ FTIR spectra of CuSb-HAB during the ECNF electrolysis.

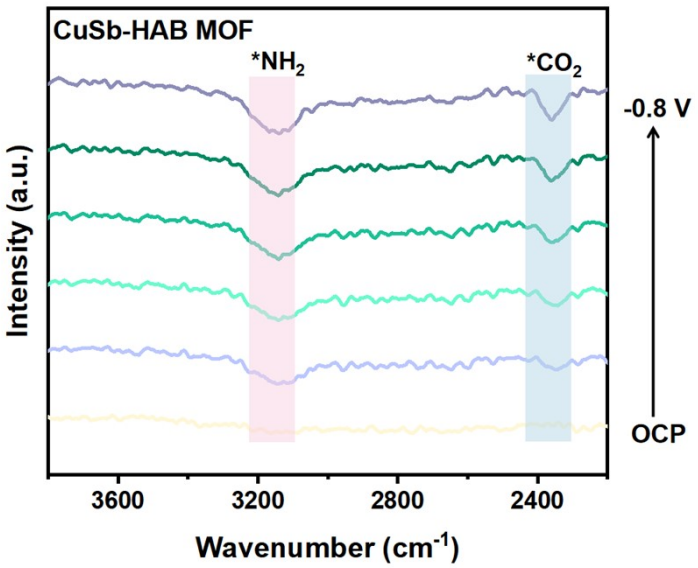

Figure S22. Potential-dependent in situ FTIR spectra of CuSb-HAB during the ECNF electrolysis.

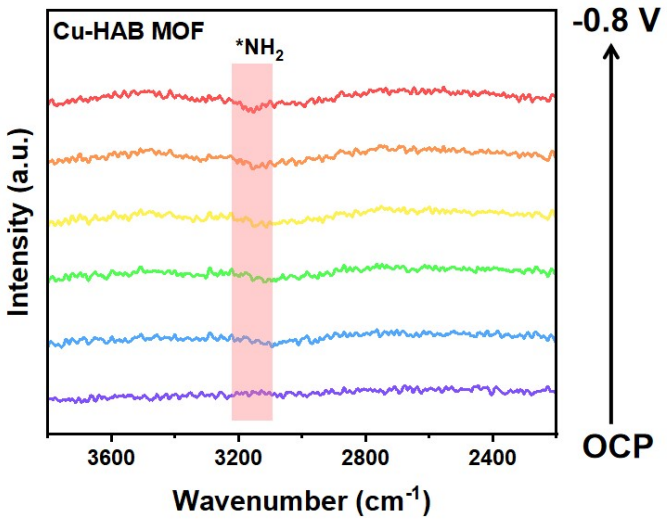

Figure S23. Potential-dependent in situ FTIR spectra of pristine Cu-HAB during the ECNF electrolysis.

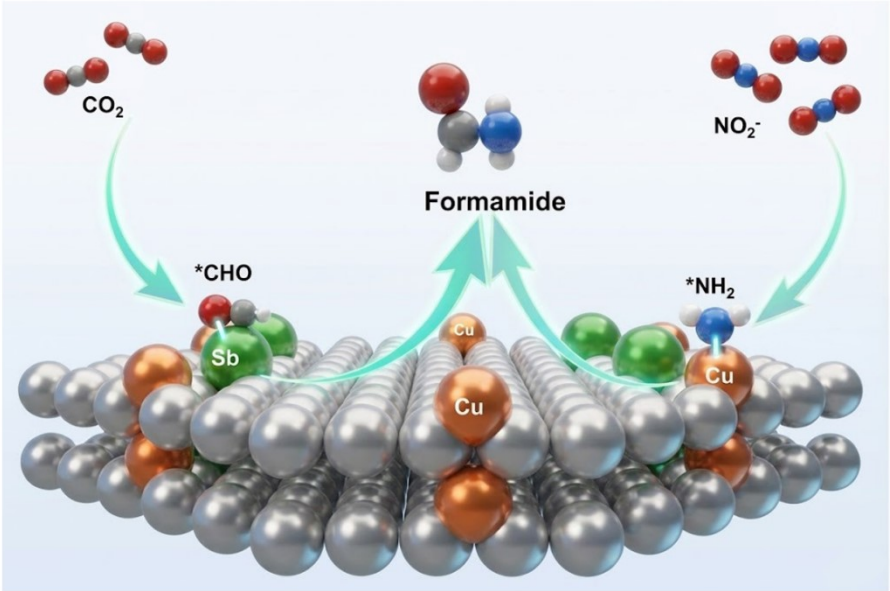

Figure S24. Schematic of the proposed ECNF pathway on CuSb-HAB.

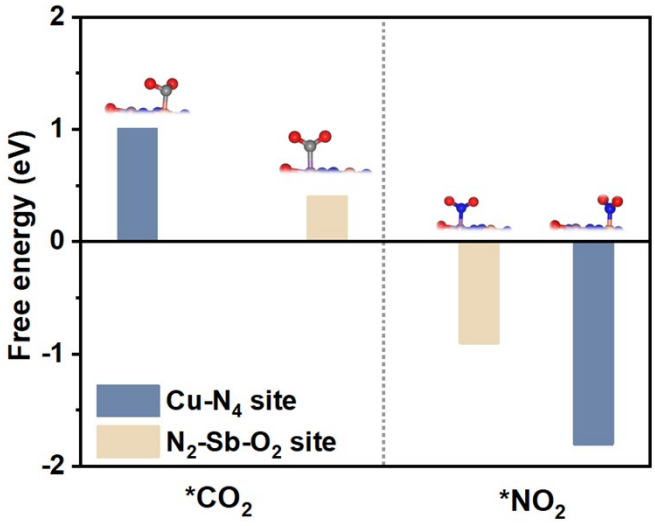

Figure S25. Adsorption free energies of *CO_2 and *NO_2 on different sites of CuSb-HAB.

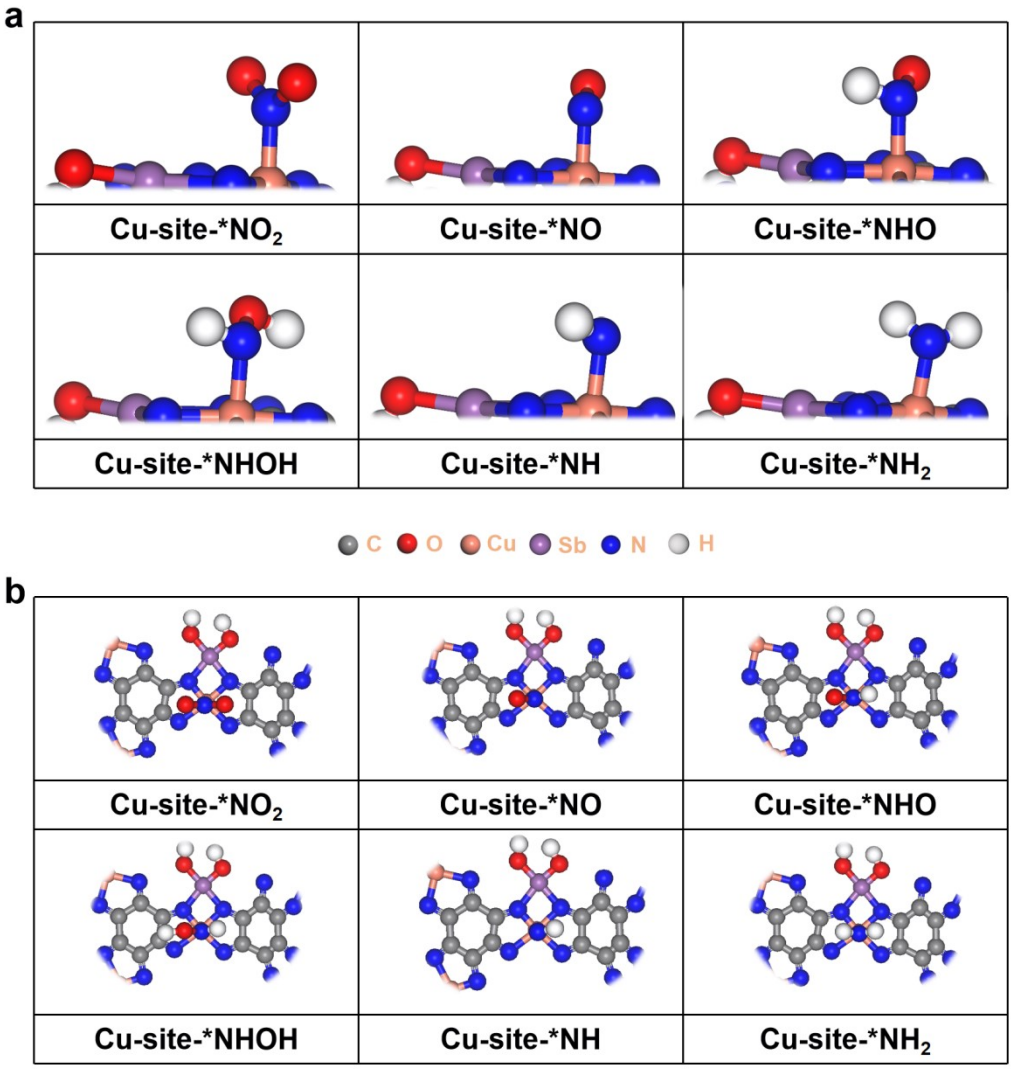

Figure S26. Optimized structures of the reaction intermediates on Cu site of CuSb-HAB along NO_2^-→*NH_2 pathway.

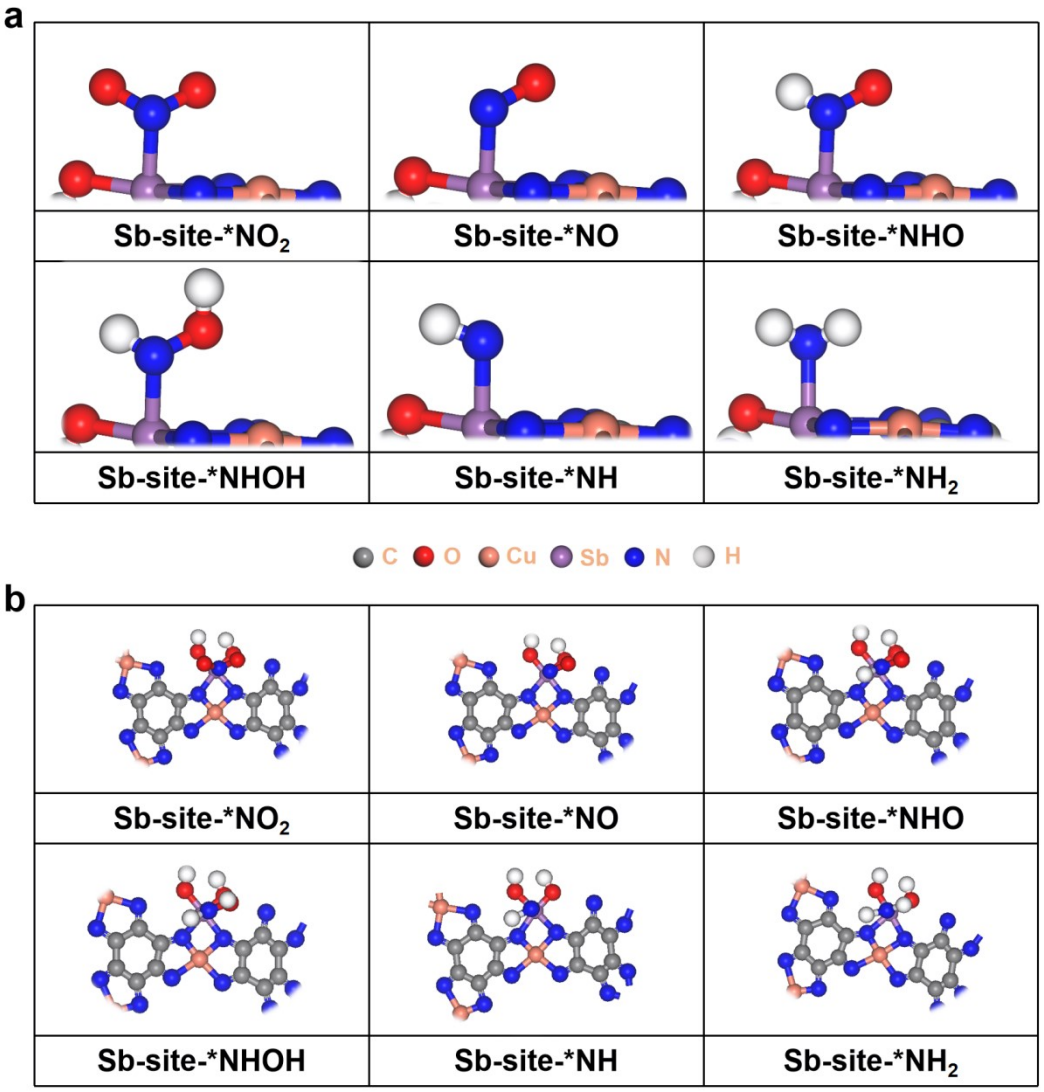

Figure S27. Optimized structures of the reaction intermediates on Sb site of CuSb-HAB along NO_2^-→*NH_2 pathway.

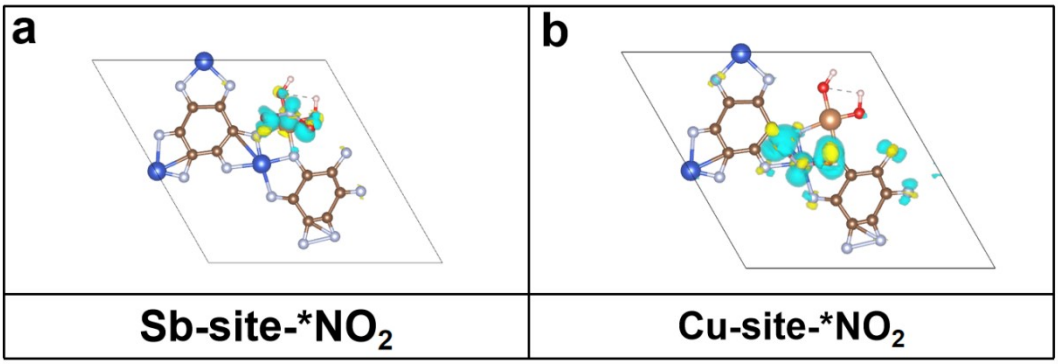

Figure S28. Electron density differences of $*NO_2$ on Cu site and Sb site of CuSb-HAB (Yellow: accumulation, cyan: depletion).

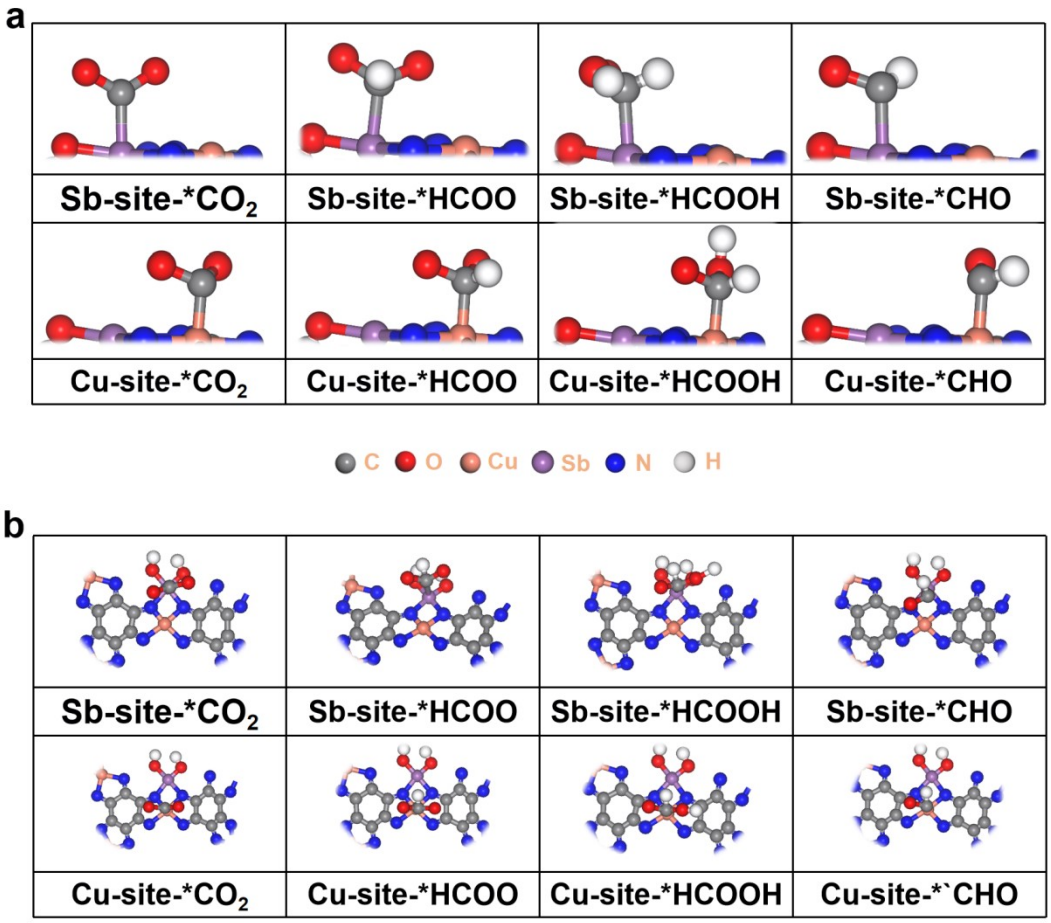

Figure S29. Optimized structures of reaction intermediates along CO_2 → *CHO pathway on Cu and Sb sites of CuSb-HAB.

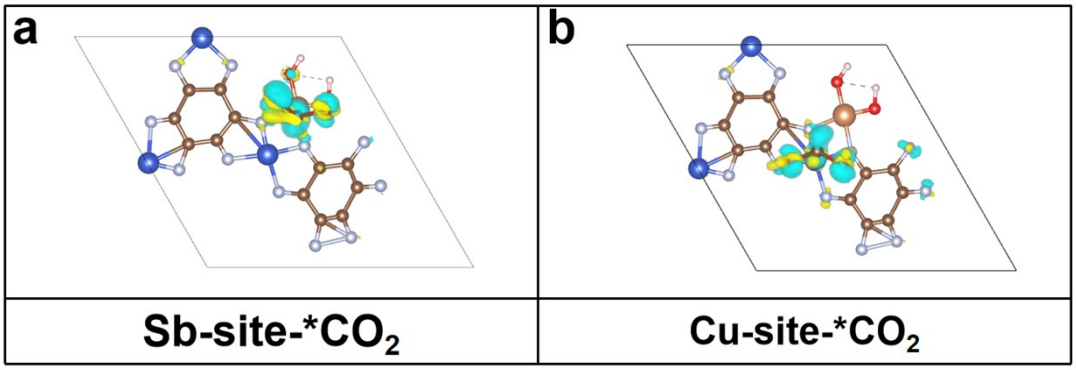

Figure S30. Electron density differences of $*CO_2$ on Cu site and Sb site of CuSb-HAB (Yellow: accumulation, cyan: depletion).

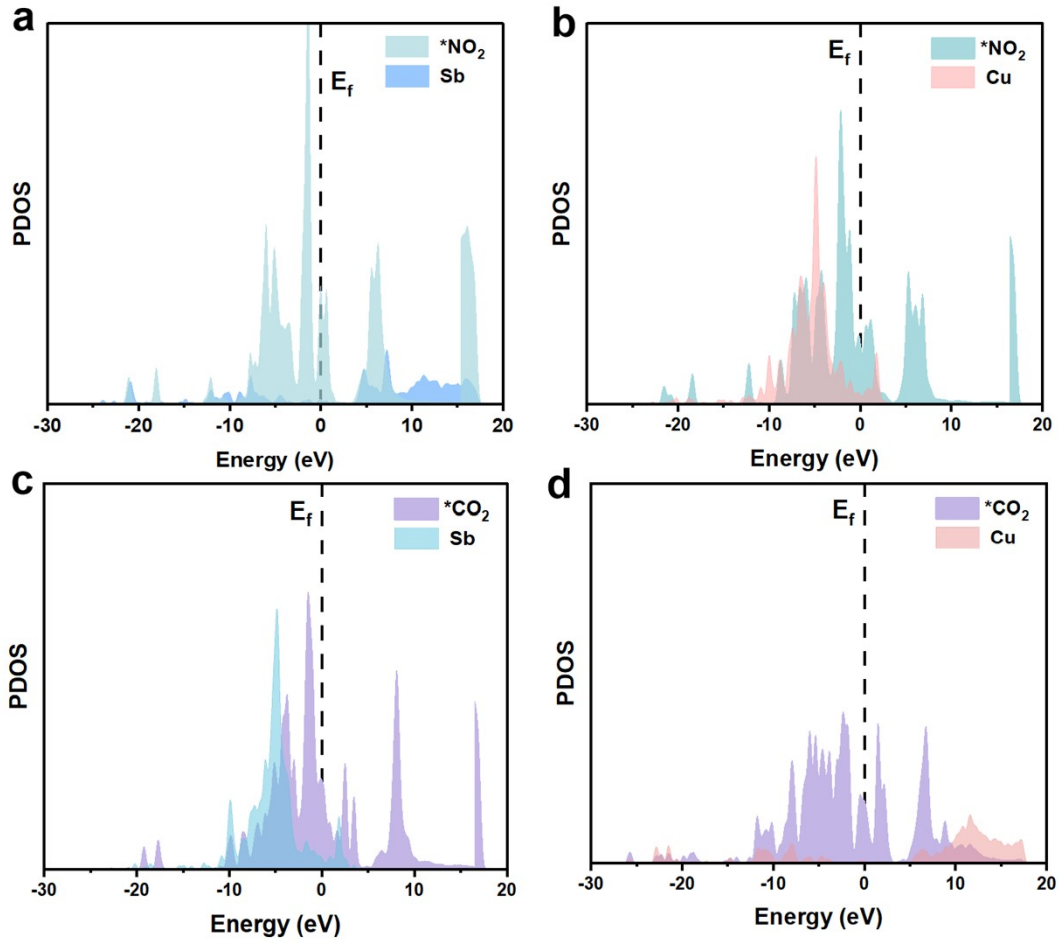

Figure S31. (a-b) PDOS profiles of adsorbed NO_2^- on Cu and Sb sites of CuSb-HAB. (c-d) PDOS profiles of adsorbed CO_2 on Cu and Sb sites of CuSb-HAB.

PDOS analysis (Figure S29a-b) shows that there is more electronic state overlapping between *NO_2 on Cu site compared to *NO_2 on Sb site of CuSb-HAB, suggesting the enhanced NO_2^- activation on Cu site. PDOS analysis (Figure S29c-d) shows that there is more electronic state overlapping between *CO_2 on Sb site compared to *CO_2 on Cu site of CuSb-HAB, suggesting the enhanced CO_2 activation on Sb site.

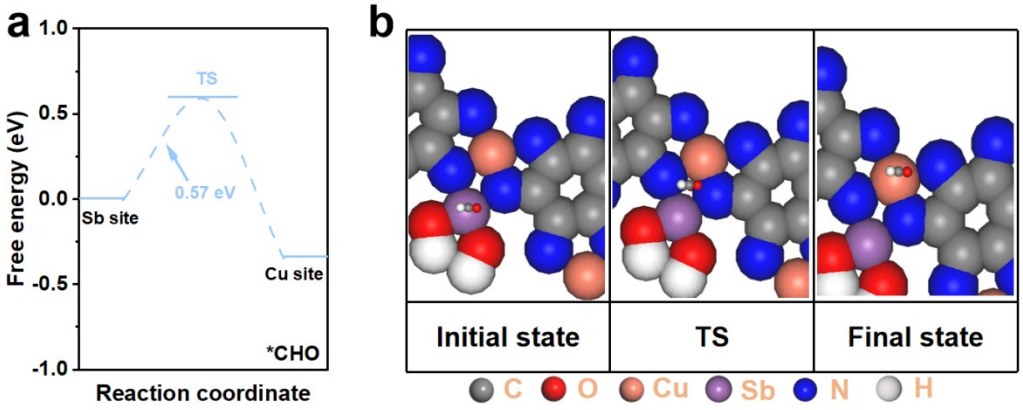

Figure S32. (a) TS energy change for *CHO migration from Sb site to Cu site, and corresponding (b) optimized intermediate structures.

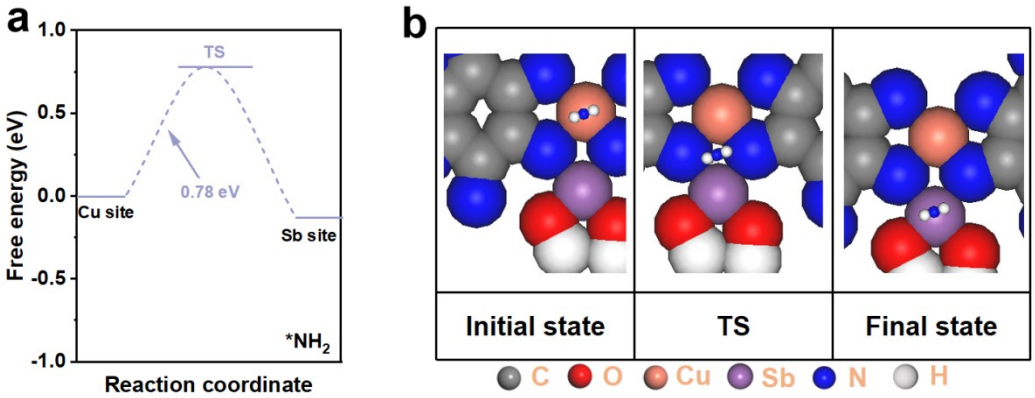

Figure S33. (a) TS free energy change for *NH_2 migration from Cu site to Sb site, and corresponding (b) optimized intermediate structures.

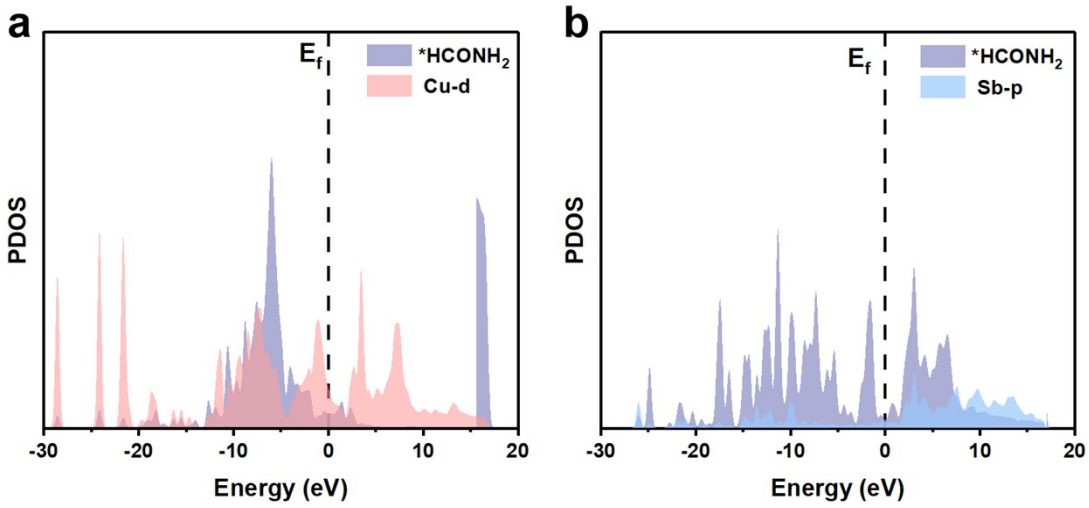

Figure S34. (a) PDOS profile of *$HCONH_2$ on Cu site of CuSb-HAB. (b) PDOS profile of *$HCONH_2$ on Sb site of CuSb-HAB.

PDOS analysis (Figure S32a-b) shows that Cu site higher degree of orbital hybridization with the formamide, particularly near the critical Fermi level, which directly results in stronger adsorption and higher catalytic activity.

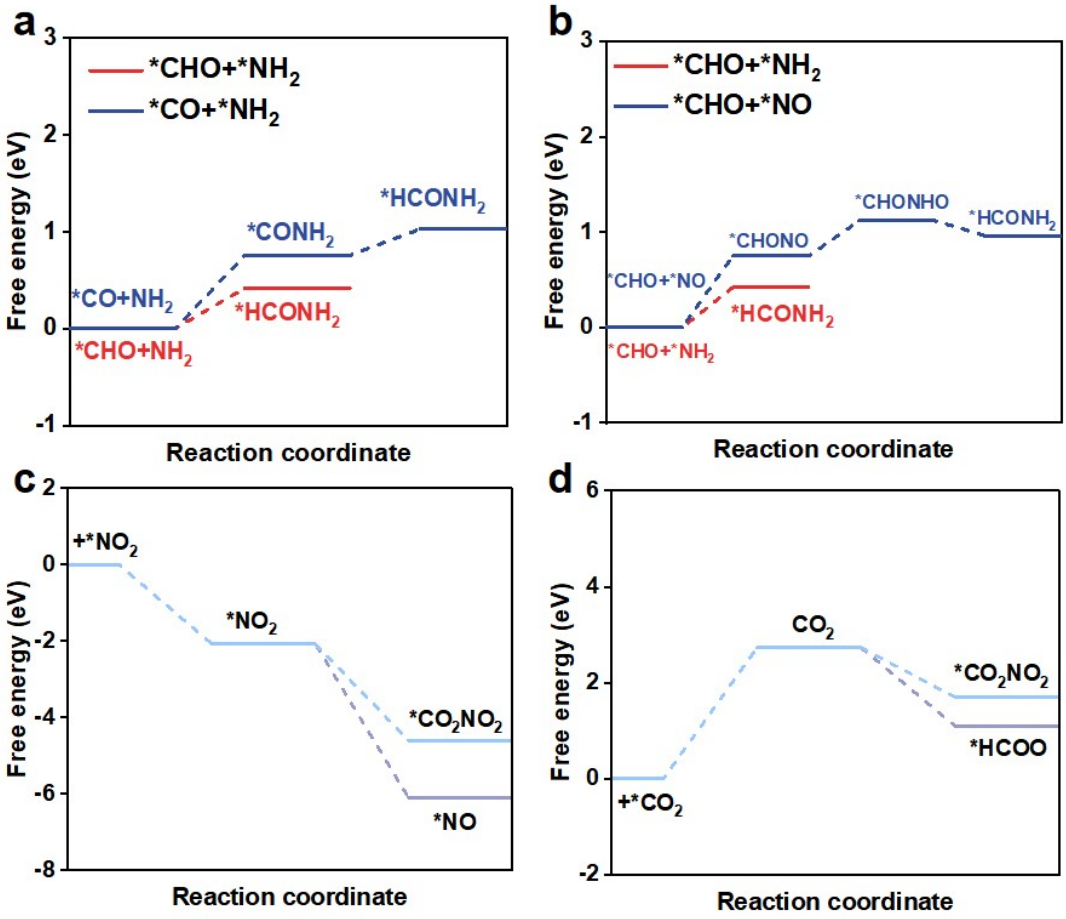

Figure S35. (a) Free energy profiles for the coupling of *CHO/*NH_2 and *CO/*NH_2 to form *$HCONH_2$. (b) Free energy profiles for the coupling of *CHO/*NH_2 and *CHO/*NO to form *$HCONH_2$. (c) Free energy profiles of *NO_2 reduction to form various intermediates. (d) Free energy profiles of *CO_2 reduction to form various intermediates.

For *NH_2 with *CO coupling process, free energy profiles that this step has a much higher energy barrier (1.03 eV) than *CHO+*NH_2 coupling, making it kinetically unfavorable. For *NH_2 with *CHO coupling process, free energy profiles show that this step has a much higher energy barrier (1.12 eV) than *CHO+*NH_2 coupling, making it kinetically unfavorable. For *NO_2→*NO process, free energy profiles show that *NO_2 prefers to be hydrogenated to form *NO intermediate rather than C-N coupling to form * CO_2NO_2 intermediate. Also, for *CO_2→*HCOO process, free energy profiles show that *CO_2 prefers to be hydrogenated to form *HCOO intermediate rather than C-N coupling to form * CO_2NO_2 intermediate.

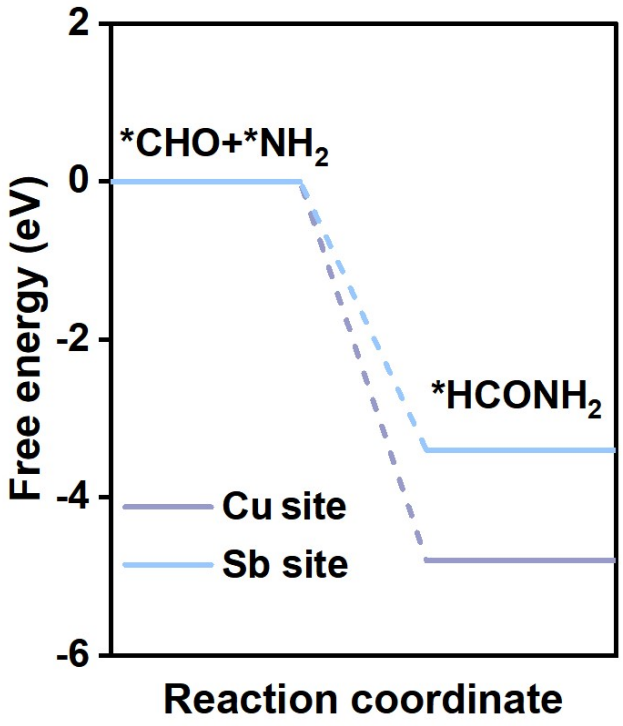

Figure S36. Free energy profiles for the coupling of *CHO and *NH_2 on Cu and Sb sites to form *$HCONH_2$.

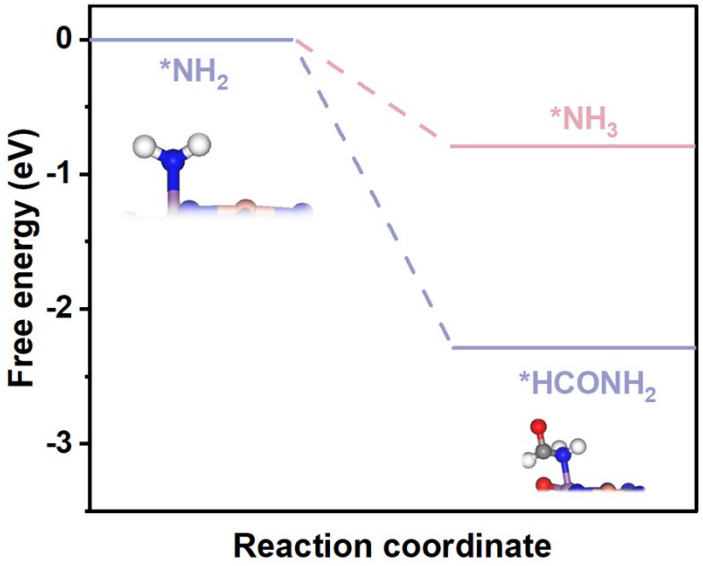

Figure S37. Free energy profiles of *NH_3 and *$HCONH_2$ formation on Cu site from CuSb-HAB.

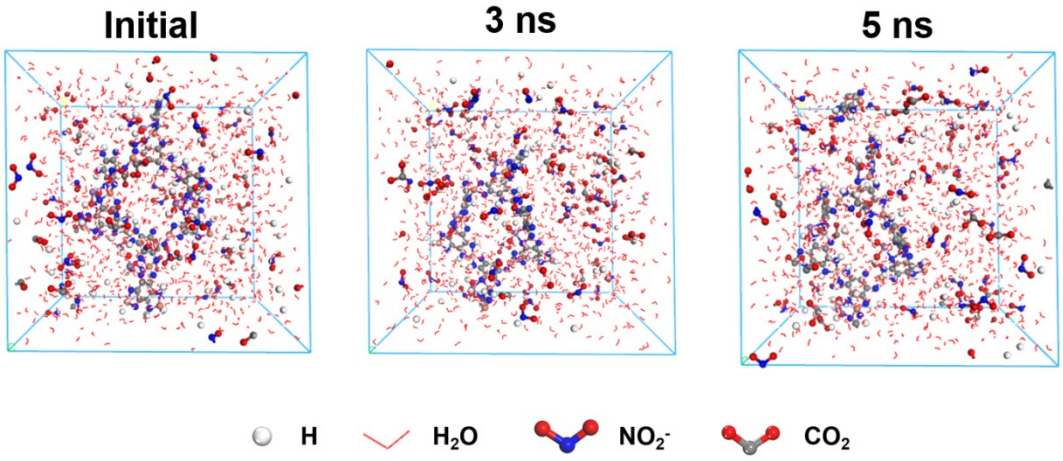

Figure S38. Snapshots for the MD dynamic process on CuSb-HAB at different simulation times.

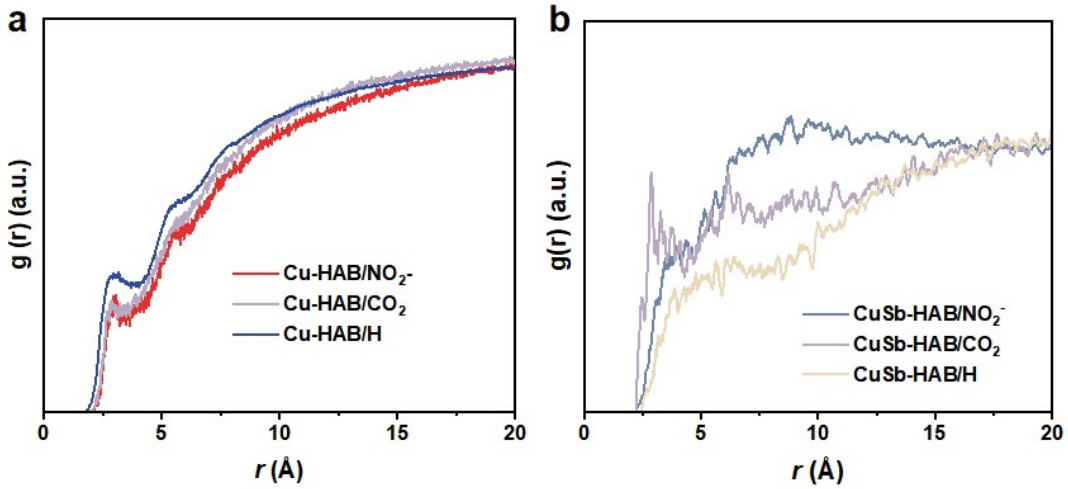

Figure S39. (a) RDF curves of the interactions between Cu-HAB and *NO_2, *CO_2, *H. (b) RDF curves of the interactions between CuSb-HAB and *NO_2, *CO_2, *H.

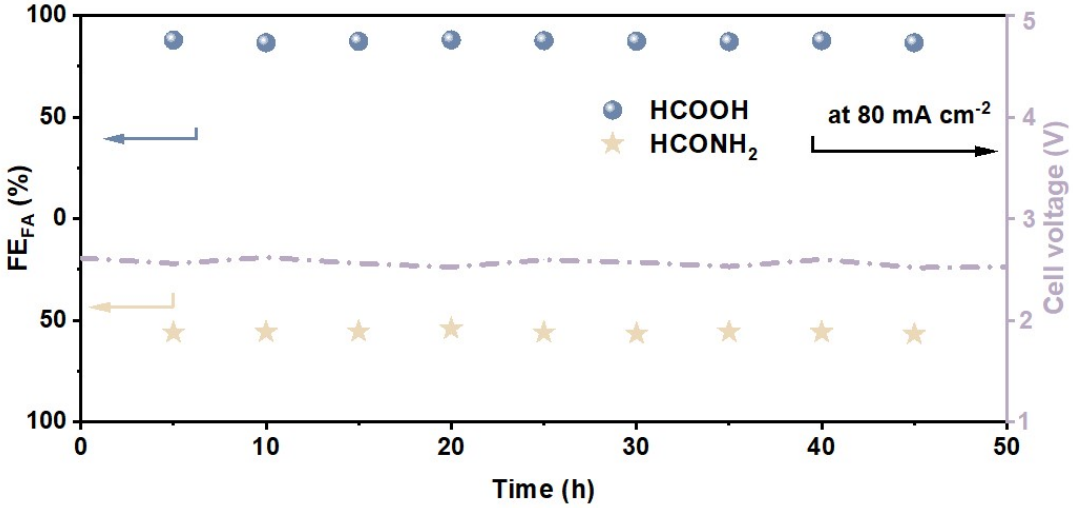

Figure S40. Long-term stability test of flow cell (ECNF||MOR) at 80 mA cm^{-2}.

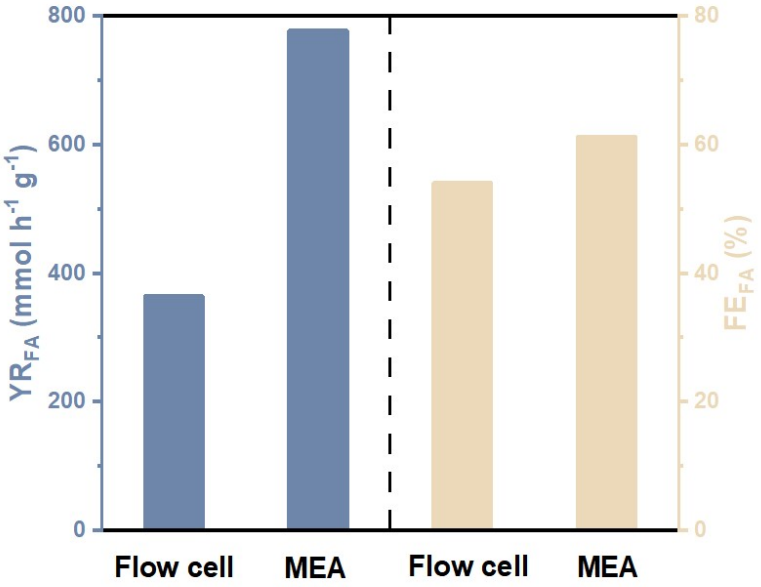

Figure S41. YR_{FA} and FE_{FA} of CuSb-HAB at 2.5 V in different cells.

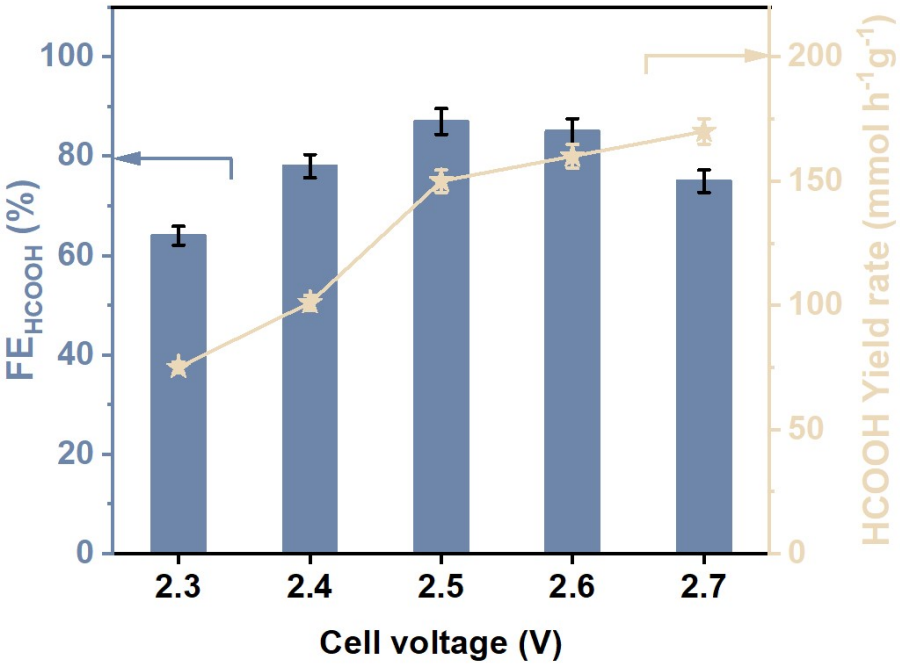

Figure S42. HCOOH yield rate/FE_{HCOOH} obtained in MEA (ECNF||MOR) at different cell voltages.

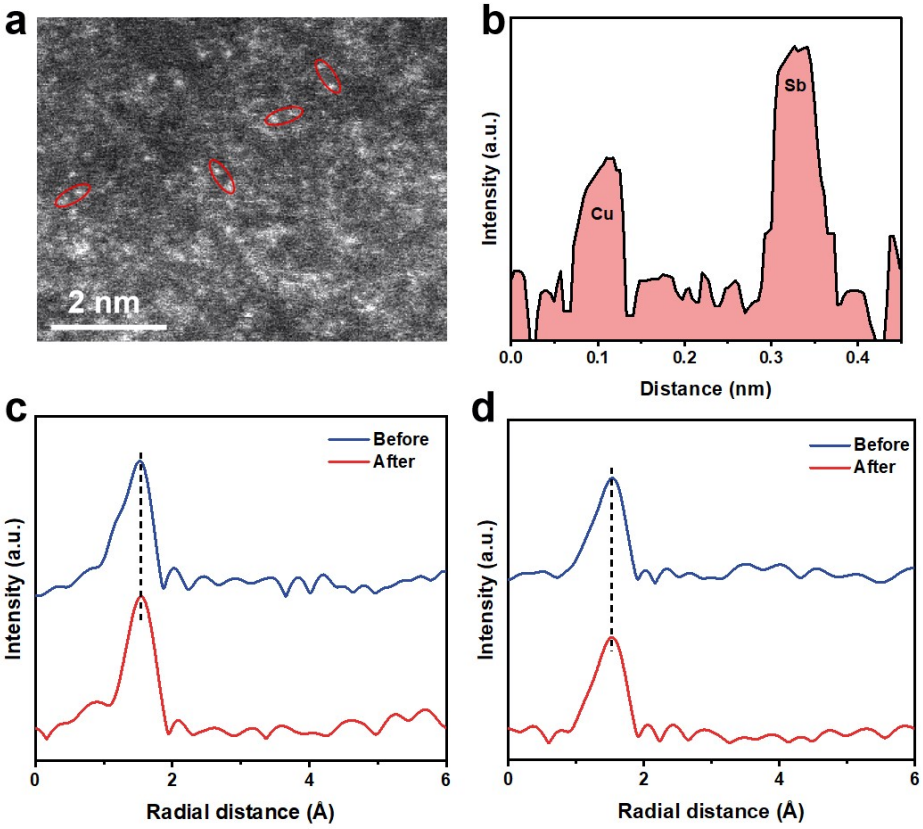

Figure S43. (a) AC-HAADF-STEM image and corresponding (b) intensity line scanning profile of CuSb-HAB after ECNF electrolysis tests. (c) Cu K-edge EXAFS of CuSb-HAB before and after ECNF electrolysis tests. (d) Sb K-edge EXAFS of CuSb-HAB before and after ECNF electrolysis tests.

The AC-HAADF-STEM image (Figure S43a-b) of CuSb-HAB after electrolysis remains largely consistent with that obtained prior to electrolysis. The absence of catalyst surface reconstruction during ECNF electrolysis corroborates the robust structural durability of CuSb-HAB. In addition, EXAFS analysis (Figure S43c) reveals that the dominant Cu-N coordination at ~1.49 Å remains unchanged after testing, with no detectable Cu-Cu or Cu-Sb interactions. Likewise, EXAFS analysis (Figure S43d) reveals that the dominant Sb-O coordination at ~1.51 Å remains unchanged after testing, with no detectable Sb-Sb or Cu-Sb interactions, indicating no leaching or aggregation of Cu and Sb dual atoms.

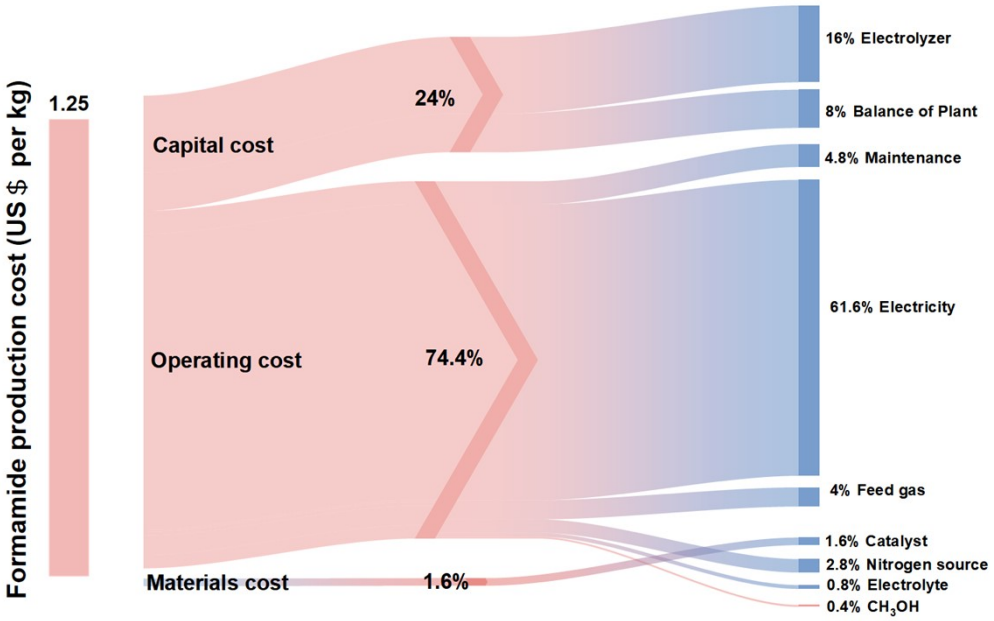

Figure S44. Estimated cost of MEA (ECNF||MOR) system for formamide synthesis.

Note S1

The TEA in this study was developed and implemented based on previously reported models. Under standard laboratory conditions (1.0 M CH_3OH in 1.0 M KOH and 0.02 M KNO_2 in 0.5 M KOH, room temperature, catalyst loading of 2 mg cm^{-2}), the baseline parameters for ECNF were selected based on the optimal performance in this study: current density of 120 mA cm^{-2}, total cell voltage of 2.5 V, and FE of 61.21 %. The target comparison cases include the use of traditional Aminolysis of Methyl Formate (reflected in formamide market prices) and nitrate wastewater treatment costs.

1. Assume that formamide production is 1000kg day^{-1}.

Required current:

$$1000\frac{kg}{day}\times\frac{day}{86400s}\times\frac{kmol}{\frac{45.04}{kg}}\times\frac{1000mol}{kmol}\times 9e^{-}\times\frac{96485C}{mol}\times\frac{1}{61.21\%}=364558.5A$$

2.Resources requirement:

$$NO_2^- =\frac{1000kg}{day}\times\frac{1kmol}{45.04kg^{-1}(formamide)}\times\frac{46kg\left(NO_2^-\right)}{1kmol}=1022.2\frac{kg}{day}$$

$$CO_2=\frac{1000kg}{day}\times\frac{1kmol}{45.04kg^{-1}(formamide)}\times\frac{44kg(CO_2)}{1kmol}=976.9\frac{kg}{day}$$

Capital Costs

1.Electrolyzer Costs: Referencing typical operating parameters for industrial electrolyzers and the DOE (U.S. Department of Energy) H2A analysis framework, the technical-economic assessment uses 300 mA cm^{-2} as the benchmark current density.

The cost of a MEA electrolyzer system is approximately 700 USD kW^{-1}, with an installation factor of 1 and an annual operating days of 330 days (allowing for 5% maintenance time). This selection is based on:

(1) Equipment cost optimization: Increasing current density reduces the investment cost per unit of production capacity for electrolysis cells

(2) Industrial practice: Commercial water electrolysis systems typically operate within the 200-400 mA cm^{-2} range

(3) Expected technological advancements: It is anticipated that engineering optimizations (such as flow design and temperature control) will enable stable operation at higher current densities.

Based on polarization curve testing, the cell voltage corresponding to 300 mA cm^{-2} is estimated to be 3.1 V. According to typical values for iR compensation in nitrate electrolyte systems: $R_s \approx 2-5\Omega \cdot cm^{-2}$

When $R_s = 3\Omega \cdot cm^{-2}$, $j = 300mA \cdot cm^{-2}$, then： $iR = 0.3A \cdot cm^{-2} \times 3\Omega \cdot cm^{-2} = 0.9V$

Then, after considering iR compensation and industrial system overpotential, it is adjusted to 2.2 V for cost calculation. Based on the effective area requirement at a current density of 300 mA cm^{-2}:

Electrolyzer area:

$$\frac{364558.5A}{0.3A \cdot cm^{-2}} \times \frac{m^2}{10^4 cm^2} = 121.5m^2$$

If the engineering margin is increased by 15%, the electrolytic cell area will be 139 m^2.

Power requirement:

$$P = UI = 2.2V \times 364558.5A \times \frac{MW}{10^6 W} = 0.80MW$$

Based on 300 mA cm^{-2} and 2.2V calculations, the total power requirement is 0.80 MW. Using a standard 0.5 m^2 single-cell design, 278 electrolysis cell units are required in parallel, with a single-cell effective area ratio of ≥15%.

Electrolytic cell cost:

$$\frac{700\ \$/kW}{1000\frac{W}{kW}} \times \frac{300mA \cdot cm^{-2}}{1000\frac{mA}{A}} \times 2.2V \times \frac{139m^2}{0.0001\frac{m^2}{cm^2}} \times 1 = 642180\ \$$$$

Considering the capital recovery factor (CRF) based on a discount rate of 5% (represented as *i* in the following equation), its lifespan is 20 years,

$$CRF = \frac{i(1+i)^{year}}{(1+i)^{year-1}} = 0.1019$$

Electrolytic cell cost:

$$642180 \times \frac{0.1019}{330day} \times \frac{1}{1000kg/day} = 0.20\ \$\ \cdot kg(formamide)^{-1}$$

2. Balance of plant (BOP) cost:

The BOP cost is assumed to be 35% of the total cost of the electrolyzer system.

BOP cost:

$$\frac{0.20\ \$\ \cdot kg(formamide)^{-1}}{65\%} \times 35\% = 0.10kg \cdot (formamide)^{-1}$$

Operating Costs

1. Electricity

Based on publicly available data from the US Energy Information Administration, calculated at an electricity price of 4 cents per kWh^{-1}.

Electricity cost:

$$0.80MW \times \frac{1000kW}{MW} \times 24h \times \frac{\$\ 0.04}{kWh} \times \frac{1}{1000kg \cdot day^{-1}} = 0.77\ \$\ \cdot kg^{-1}$$

2. Equipment maintenance, assuming maintenance costs are 3% of the capital cost of the electrolytic cell (including membrane replacement cycle and catalyst life).

Maintenance cost:

$$642180 \times \frac{3\%}{year} \times \frac{year}{330days} \times \frac{1}{1000kg \cdot day^{-1}} = 0.06\$ \cdot kg^{-1}$$

3. CH_3OH

Assuming that the cost of CH_3OH is 2% of the cost of the electrolytic cell

CH_3OH cost:

$$0.20 \times 2\% = 0.004\$ \cdot kg(formamide)^{-1}$$

4. Electrolyte

Assuming that the cost of electrolyte is 5% of the cost of the electrolytic cell

electrolyte cost:

$$0.20 \times 5\% = 0.010\$ \cdot kg(formamide)^{-1}$$

5.Raw gas cost

If CO_2 is purchased externally, according to the CCUS project (including capture and compression), the price of high-concentration CO_2 capture is \$0.08/kg.

Raw gas cost:

$$\frac{976.9kg}{day} \times \frac{\$0.08}{kg} \times \frac{1}{1000kg \cdot day^{-1}} = 0.05\$ \cdot kg(formamide)^{-1}$$

6. NO_2^- electrodialysis cost:

When NO_2^- needs to be pre-concentrated by electrodialysis before being sent to the MEA cell, the cost of the electrodialysis process is based on the biological denitrification cost of \$1.6/kg NO_2^- at the California Municipal Wastewater Treatment Plant in the United States.

Nitrogen source cost:

$$1022.2\frac{kg}{day} \times \frac{\$1.6}{kmol} \times \frac{1kmol}{46kg} \times \frac{1}{1000kg \cdot day^{-1}} = 0.035\$ \cdot kg(formamide)^{-1}$$

Material costs

Assume that material costs account for 10% of the cost of the electrolytic cell.

Catalyst cost:

$$0.2 \times 10\% = 0.02\$ \cdot kg(formamide)^{-1}$$

Sensitivity analysis

Range of fluctuations in key parameters:

Parameters	Reference value	Range of variation
Current density	300 mA cm^{-2}	±15 %
FE	61.21 %	±10 %
Electricity price	0.04 \$/kWh	0.03-0.05 \$/kWh

Although laboratory optimization achieved the best FE at 120 mA cm^{-2}, industrial-grade TEA uses 300 mA/cm^2 as the benchmark. This choice:

(1) aligns with the industry's technological development trajectory

(2) provides a more realistic cost prediction framework

(3) reserves sufficient safety margins for subsequent engineering scaling

The calculated formamide cost price derived from the above analysis is 1.25 $ kg (formamide)$^{-1}$, which is higher than the current industrial production cost price for formamide. However, if a multi-product system is used (i.e., directly obtain formic acid at the anode), extracting nitrates from wastewater and pre-treating them, then transferring them to an electrolytic cell for electrocatalytic reactions, while sharing auxiliary equipment such as pipelines and valves can reduce the capital investment. Additionally, wastewater treatment fees can be saved through the multi-product system, Use the formic acid produced at the anode as a supplement to the formic acid at the cathode, or sell the formic acid that can be obtained through trading. By implementing the above methods, the total cost can be reduced, bringing the formamide cost price close to or even below the market price, achieving economic viability, and potentially becoming a new path for wastewater resource utilization and Specialty chemical products in the future.

Table S1. Compositions of CuSb(5/1)-HAB measured by ICPMS.

Sample	**Cu (wt%)**	**Sb (wt%)**	**Cu/Sb mole ratio**
CuSb(5:1)**-HAB**	32.5	6.67	5:1

Table S2. Cu K-edge and Sb K-edge EXAFS fitting results of CuSb-HAB.

Sample	Shell	CN	R (Å)	σ^2 (10^{-3}Å)	$\lvert\Delta E_0\rvert$ (eV)	R factor
CuSb-HAB	Cu-N	1.9	1.98	4.3	6.7	0.12
	Sb-O	2.1	2.02	3.5	5.8	0.08

CN is the coordination number, R is interatomic distance, σ^2 is Debye-Waller factor, ΔE_0 is edge-energy shift, R factor is used to value the goodness of the fitting.

Table S3. Comparison of the optimum YR_{FA} and FE_{FA} for the recently reported state-of-the-art ECNF electrocatalysts at ambient conditions.

Catalyst	Reactant	Electrolyte	yield rate	FE_{FA} (%)	Potential (V vs RHE)	Cell	Ref.
ER-Cu	$HCOOH + NO_2^-$	0.5 M NaOH + 0.2 M HCOOH+ 0.02 M $NaNO_2$	35.1 $mmolh^{-1}$ g_{cat}^{-1}	29.7	-0.6	H cell	4
Cu	$CO_2 + NH_4OH$	CO_2 + 1 M KOH + 1 M NH_4OH	/	0.30	-0.98	GDE	5
Ru_1Cu	$CO + NO_2^-$	CO_2 + 1 M KOH + 1 M KNO_2	2483.77 μg h^{-1} mg_{cat}^{-1}	45.65	-0.5	H cell	6
CuO_x/BiO_x	$CO_2 + NO_2^-$	CO_2 + 0.2 M $KHCO_3$ + 0.02 M KNO_2	134 mmol h^{-1} $g_{cat}t^{-1}$	3.30	-1.2	Flow cell	7
Pt foil	$EG+NH_3$	4.0 M EG + 1.0 M NH_3 + 0.5 M $KHCO_3$	1003.63 μmol $cm^{-2}h^{-1}$	55.87	1.8	MEA	8
WO_3	$EG+NH_3$	0.25 M H_2SO_4+EG+NH_3 (1:1 vol.ratio)	537.7 μmol cm^{-2} h^{-1}	43.2	2.0	MEA	9
Pt-Ti	CH_3OH+NH_3	0.5M $NaHCO_3$+CH_3OH + NH_3 (4:1 vol.ratio)	305.4 μmol cm^{-2} h^{-1}	40.39	1.3	Flow cell	10
1%Pr-MnO_2	CH_3OH+NH_3	0.5M $NaHCO_3$+CH_3OH + NH_3 (2:1 vol.ratio)	211.32 μmol cm^{-2} h^{-1}	22.63	/	Flow cell	11
CuO/In_2O_3	CH_3OH+NH_3	0.25 M Na_2SO_4+CH_3OH + NH_3 (4:1 vol.ratio)	8.43 ± 1.54 g h^{-1} mg_{cat}^{-1}	49.05	1.5	H cell	12
F-Nb_2O_5/CP	CH_3OH+NH_3	0.5M $NaHCO_3$+CH_3OH + NH_3 (8:1 vol.ratio)	99 μmol cm^{-2} h^{-1}	52.0	1.5	H cell	13
CuSb-HAB	$CO_2 + NO_2^-$	CO_2 + 0.2 M $KHCO_3$ + 0.02 M KNO_2	376 mmol h^{-1} $g_{cat}t^{-1}$	54.9	-0.8	Flow cell	**This work**
CuSb-HAB	$CO_2 + NO_2^-$	CO_2 + 0.2 M $KHCO_3$ + 0.02 M KNO_2	777.9 mmol h^{-1} $gcat^{-1}$	61.21	-0.8	MEA	**This work**

References

1. Y. Huang, R. Yang, C. Wang, N. Meng, Y. Shi, Y. Yu and B. Zhang, ACS Energy Lett., 2021, 7, 284-291.
2. P. Li, Z. Jin, Z. Fang and G. Yu, Energy Environ. Sci., 2021, 14, 3522-3531.
3. Z.-Y. Wu, M. Karamad, X. Yong, Q. Huang, D. A. Cullen, P. Zhu, C. Xia, Q. Xiao, M. Shakouri and F.-Y. Chen, Nat. Commun., 2021, 12, 2870.
4. C. Guo, W. Zhou, X. Lan, Y. Wang, T. Li, S. Han, Y. Yu and B. Zhang, J. Am. Chem. Soc., 2022, 144, 16006-16011.
5. J. Li and N. Kornienko, Chem. Sci., 2022, 13, 3957-3964.
6. J. Lan, Z. Wei, Y.-R. Lu, D. Chen, S. Zhao, T.-S. Chan and Y. Tan, Nat. Commun., 2023, 14, 2870.
7. P. Ramadhany, T. Trần-Phú, J. A. Yuwono, Z. Ma, C. Han, T. K. A. Nguyen, J. Leverett, P. Kumar, R. K. Hocking and A. Tricoli, Adv. Energy Mater., 2024, 14, 2401786.
8. X. Wang, Y. Su, J. Chen, E. H. Yan, Q. Xia, J. Wu, S. Gong, M. Tang, W. S. Yip and Y. Mu, Nat. Commun., 2025, 16, 8040.
9. Q. Shi, W. Tang, K. Kong, X. Liu, Y. Wang and H. Duan, Angew. Chem. Int. Ed., 2024, 63, e202407580.
10. N. Meng, J. Shao, H. Li, Y. Wang, X. Fu, C. Liu, Y. Yu and B. Zhang, Nat. Commun., 2022, 13, 5452.
11. J. Zhu, J. Shao, B.-A. Shen, J. Chen, Y. Yu, S. Song, X.-B. Zhang, B. Zhang and B.-H. Zhao, JACS Au, 2023, 3, 2987-2992.
12. Q. Shen, W. Chen, Z. Wei, J. Tan, M. Wang, Y. Qiao, L. Zhang and J. Shi, Appl. Catal. B Environ., 2025, 125581.
13. S. Mou, S. Liu, W. Dai, Y. Sun and F. Dong, Appl. Catal. B Environ., 2025, 365, 124963.